ACS OMEGA

http://pubs.acs.org/journal/acsodf

Article

Magnetic Ti_3C_2 MXene Nanomaterials for Doxorubicin Adsorption from Aqueous Solutions: Kinetic, Isotherms, and Thermodynamic Studies

Dan Liu,* Tongyi Li, Wenjie Sun, Wenjuan Zhou, and Guohua Zhang

Cite This: *ACS Omega* 2022, 7, 31945−31953

Read Online

ACCESS | Metrics & More | Article Recommendations

ABSTRACT: In this work, the magnetic Ti_3C_2 MXene functionalized with β-cyclodextrin was prepared and characterized using scanning electron microscopy, transmission electron microscopy, Fourier transform infrared spectra, X-ray diffraction, X-ray photoelectron spectroscopy, vibrating sample magnetometry, and thermogravimetric analysis. The synthesized nanomaterial was used as an adsorbent to adsorb doxorubicin from aqueous solutions, and the experimental parameters that affected the adsorption efficiency were investigated. In addition, the adsorption characteristics including adsorption kinetics, adsorption isotherm, and thermodynamics were researched comprehensively. The adsorption kinetics of doxorubicin followed a pseudo-second-order kinetic model, which indicated that adsorption was the rate-limiting step, and the maximum adsorption capacity was 7.35 $\mu g\ mg^{-1}$ by shaking for 60 min at pH 7.0. The adsorption isotherm was well described using the Freundlich model, which implied that multilayer adsorption took place over the prepared nanomaterial for doxorubicin adsorption. The negative values of Gibbs free energy change ($\Delta G^0 < 0$) demonstrated that doxorubicin adsorption was a spontaneous process. The positive values of entropy change ($\Delta S^0 > 0$) implied that doxorubicin adsorption was an increasing random process. Enthalpy change values were positive ($\Delta H^0 > 0$) and indicated that the adsorption of doxorubicin was endothermic. The adsorption percentage of doxorubicin remained in the range of 41.05−44.09%, and the relative standard deviation (RSD) based on the adsorption percentage through five replicate adsorption and desorption processes was 2.8%. These results indicated that the magnetic Ti_3C_2 MXene nanomaterials can be an effective adsorbent to adsorb DOX from aqueous solutions.

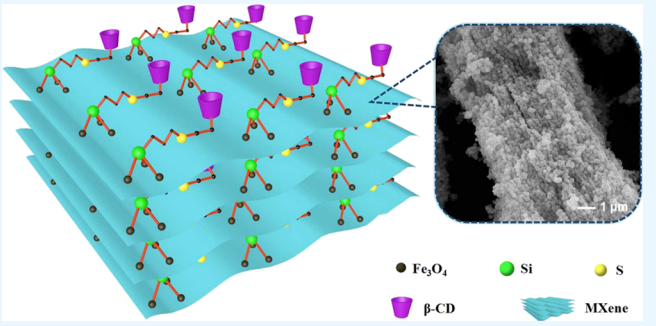

1. INTRODUCTION

In recent years, two-dimensional (2D) structure materials have shown unique physical and chemical properties compared with other materials. MXene (e.g., $Ti_3C_2T_x$), a family of 2D materials, has attracted wide interest since its discovery in 2011[1] because of its relatively large specific surface area, high electrical conductivity, and hydrophilicity.[2] The general formula of MXene is often described as $M_{n+1}X_nT_x$ (M, X, and T_x represent a transition metal, carbon/nitrogen, and surface functional groups such as −OH, −O, and −F),[3] and they are produced by selective etching of IIIA or IVA elements from the MAX phase (e.g., Ti_3AlC_2).[4,5] MXene has shown huge potential in multiple fields, such as sensors, energy storage, cancer therapy, and EM wave absorption and shielding. Because of the large specific surface area, hydrophilic performance, tunable surface chemistry, high negative zeta potential, and environment-friendly characteristics, MXene has attracted wide attention in adsorption and remediation of wastewater.[6] For example, Ti_3C_2 MXene exhibited a high adsorption efficiency with the removal rate enhanced up to ∼99.7% for ciprofloxacin from wastewater,[7] which revealed that MXenes can be used as a novel adsorption nanomaterial with great potential in environmental applications.[8]

Doxorubicin (DOX) is an effective anticancer drug, which can significantly inhibit the growth of tumor cells. However, it will lead to a variety of adverse side effects and multidrug resistance effects in cancer treatments because it cannot distinguish between normal cells and tumor cells.[9] Eventually, after administration to patients, it may be released into the environment through excretions as mixtures of its original form and their metabolites.[10] The detection of DOX in oncologic hospital wastewater in some areas was in the range of 0.26−1.35 $\mu g\ L^{-1}$,[11] and 0.02−0.042 $\mu g\ L^{-1}$ was detected in

Received: May 6, 2022
Accepted: August 22, 2022
Published: September 1, 2022

wastewater treatment plants.[12] Eco-genotoxicity studies revealed that DOX causes DNA damage to *Ceriodaphnia dubia* cells at a concentration of 0.05 μg L^{-1}. Thus, DOX has been one of the contaminants in the list of emerging substances because of the potential risks.[13] The solubility of DOX is extremely low in neutral water and could pose harmful effects on growing eukaryotic organisms because of its toxicity, genotoxicity, mutagenicity, and teratogenicity.[14] Various treatment methods such as membrane technology, activated carbon, exchange resins method, and advanced oxidation technology have been tried for the elimination of pharmaceutical residues from water.[13,15,16] Unfortunately, secondary pollutants may be formed in aqueous solutions because of the complex structures and variable physicochemical properties of DOX.[17,18] Accordingly, it is necessary to find a more effective method for removing DOX.

Adsorption technology is considered to be a promising method for removing pollutants from effluents.[14] More kinds of absorbents such as carbon nitride, carbon nanotubes, and graphene nanoribbons have been used for adsorption of DOX from aqueous solutions,[19−21] but some shortcomings such as time consumption and difficult separation exist.[18] Recently, iron oxide nanoparticles (Fe_3O_4 NPs) have attracted extensive attention in the field of environmental remediation.[22,23] However, unmodified Fe_3O_4 NPs are difficult to recycle in practical application because they are easy to agglomerate and form clusters.[24] Up to now, various magnetic adsorbents that were modified or coated different groups on the surface of Fe_3O_4 NPs to provide functionality and stability have been prepared for inorganic, organic, and biological analysis.[25,26] For example, multilayer cucurbit[6]uril-based magnetic nanoparticles were prepared based on host-guest interactions by Jia's group, and the compound was successfully used as a blood purification material to remove lipoprotein from plasma.[27]

β-cyclodextrin (β-CD) is a kind of nontoxic cyclic oligosaccharides, and the most significant structure is hydrophilic exterior and hydrophobic interior cavity.[28,29] It is well known that β-CD can form stable host-guest inclusion complex with a variety of aromatic molecules into its hydrophobic cavity though host-guest interactions.[30] However, the inherent solubility of β-CD hinders its practical application in a variety of areas.[31] β-CD has many reactive hydroxyl groups with high chemical reactivity, which offer abundant active centers for the reaction with organic functional groups, making it possible for new functionalization.[29] Furthermore, chemical modification can be conducted at the upper and lower edges to improve solubility and inclusion efficiency and further to construct various functional materials.[32]

In this study, magnetic Ti_3C_2 MXene functionalized with β-CD was prepared (Ti_3C_2@Fe_3O_4@β-CD) and used as an adsorbent for adsorption of DOX from aqueous solutions. The experimental parameters that affected the adsorption efficiency were investigated, and the experimental data were analyzed based on adsorption kinetics, adsorption isotherm models, and thermodynamics. After that, the performance of interference and regeneration was also investigated.

2. EXPERIMENTAL SECTION

2.1. Materials. Ti_3AlC_2, β-cyclodextrin (β-CD), hydrofluoric acid (HF), doxorubicin (DOX), allyl bromide, p-toluenesulfonyl chloride (TsCl), ethylene glycol, dimethylsulfoxide (DMSO), ferric chloride hexahydrate ($FeCl_3{\cdot}6H_2O$), ammonium hydroxide ($NH_3{\cdot}H_2O$, 25%, w/w), (3-mercaptopropyl) triethoxysilane (MPTMS), and polyethylene glycol (PEG-2000, M_n = 2000) were obtained from Macklin Reagent (Shanghai, China). Acetic acid, sodium chloride (NaCl), hydrochloric acid (HCl), sodium acetate, sodium hydroxide (NaOH), phosphoric acid (H_3PO_4), nitric acid (HNO_3), sodium hydrogen phosphate (Na_2HPO_4), sodium dihydrogen phosphate (NaH_2PO_4), and ethanol were purchased from Jiangsu Qiangsheng Chemical Co., Ltd. (Changshu, China). The DOX stock solution (100 μg mL^{-1}) was prepared by deionized water. The grade of NdFeB strong magnet is N35, and the residual magnetic flux density is 11,700−12,200 Gs.

2.2. Methodology. The synthesized magnetic nanoparticles were characterized using scanning electron microscopy (SEM, S-4800, JEOL Company, Japan; QUANTA-250, Thermo, USA), transmission electron microscopy (TEM, H-7800, Hitachi, Japan), Fourier transform infrared (FT-IR, IS10, Thermo, USA) spectrometry, X-ray diffraction (XRD, X'PERT POWDER, PANalytical B.V., Netherland), X-ray photoelectron spectroscopy (XPS, D8 Advance, Bruker), vibrating sample magnetometry (VSM, MPMS SQUID XL-7, Quantum Design, USA), and thermogravimetric analysis (TGA, STA2500, Netzsch, Germany). In addition, the concentration of DOX was determined by measuring the absorbance using a UV−visible spectrophotometer (CARY100, Agilent, USA) at a wavelength of 483 nm.

2.3. Preparation of Ti_3C_2 MXene Nanosheets. Ti_3AlC_2 (1.0 g) was slowly added in HF (10 mL) to stir for 48 h at 50 °C for complete removal of the Al layers. Then, the solution was centrifuged and rinsed several times with deionized water to remove the unreacted HF until pH > 6.0. Then, the obtained Ti_3C_2 powder was vacuum-dried at 40 °C.

2.4. Preparation of Fe_3O_4 NPs. Fe_3O_4 NPs were prepared according to our previous work.[33] $FeCl_3{\cdot}6H_2O$ (2.7 g) was added to a flask and dissolved with ethylene glycol (50 mL). After stirring violently for 30 min, the color of the solution changed from colorless to orange. Then PEG-2000 (2.0 g) and sodium acetate (7.2 g) were added to the solution and stirred for 1 h. The brown sticky solution was transferred into a Teflon-lined stainless-steel autoclave and sealed, and the autoclave was heated to 200 °C for 9 h. After that, the obtained black precipitate was washed several times with ethanol and deionized water until neutral and was dried at an ambient temperature in vacuum.

2.5. Preparation of Ti_3C_2@Fe_3O_4@β-CD. Ti_3C_2 MXene (100 mg) and Fe_3O_4 NPs (50 mg) were dispersed in 80 and 20 mL of deionized water, respectively, and allowed to stir for 30 min. Then, the above solution was mixed and ultrasound-treated for 120 min under N_2. After that, the resulting black precipitate was collected using an NdFeB strong magnet and washed several times with ethanol and deionized water. Finally, Ti_3C_2@Fe_3O_4 was obtained and dried at 50 °C overnight.

Ti_3C_2@Fe_3O_4@MPTMS was obtained with the surface of Ti_3C_2@Fe_3O_4 modified via the grafting of MPTMS as an organosilane. Ti_3C_2@Fe_3O_4 (0.1 g) was redispersed into the solution of DMSO/MPTMS (v/v, 80:2), and the mixture was stirred for 5 h at 80 °C to obtain Ti_3C_2@Fe_3O_4@MPTMS.

Allyl-β-CD was synthesized according to Zheng's work.[34] Then, Ti_3C_2@Fe_3O_4@β-CD magnetic nanomaterials were prepared by thiol-ene click reaction between −SH of MPTMS and C═C of allyl-β-CD. allyl-β-CD, Ti_3C_2@Fe_3O_4@MPTMS, and AIBN (1 wt %) was added to the DMSO, and the mixture was allowed to stir for 4 h at 75 °C. The obtained Ti_3C_2@Fe_3O_4@β-CD magnetic nanomaterials

https://doi.org/10.1021/acsomega.2c02772
ACS Omega 2022, 7, 31945−31953

were separated using an NdFeB strong magnet and then washed with ethanol and deionized water several times. The obtained products were dried under vacuum at 60 °C overnight. The synthesis process of Ti_3C_2@Fe_3O_4@β-CD was illustrated in Figure 1.

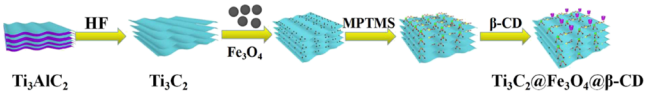

Figure 1. Synthesis of Ti_3C_2@Fe_3O_4@β-CD.

2.6. Adsorption Experiments. The DOX adsorption process onto the Ti_3C_2@Fe_3O_4@β-CD was conducted as follows: Ti_3C_2@Fe_3O_4@β-CD (5 mg) was mixed with DOX solution (15 mL, 5 μg mL^{-1}), and then, the mixture was mechanically shaken for 60 min at 25 °C. The DOX-adsorbed Ti_3C_2@Fe_3O_4@β-CD was separated using an NdFeB strong magnet. To evaluate the amount of adsorbed DOX, the adsorption percentage was measured using a UV−visible spectrophotometer at 483 nm.

The adsorption percentage of DOX was calculated according to the eq 1.

$$\text{Adsorption}\ (\%) = \frac{C_0 - C_e}{C_0} \times 100\% \quad (1)$$

where C_e and C_0 are the equilibrium concentrations and initial concentrations (μg mL^{-1}), respectively.

In order to research and construct the adsorption isotherm of DOX onto the Ti_3C_2@Fe_3O_4@β-CD, a series of concentrations of 2, 4, 6, 8, 10, 20, 30, 50, 80, and 100 μg mL^{-1} DOX standard solutions (pH 7.0) were prepared and individually mixed with Ti_3C_2@Fe_3O_4@β-CD (5 mg). The mixture was mechanically shaken for 60 min at 25 °C, and the adsorption capacity (Q_e) at equilibrium for DOX onto the Ti_3C_2@Fe_3O_4@β-CD was calculated as eq 2:[35]

$$Q_e = \frac{(C_0 - C_e) \times V}{m} \quad (2)$$

where Q_e is the adsorption capacity at equilibrium (μg mg^{-1}), V is the volume of solution in (mL), and m is the mass of the adsorbent (mg).

The kinetic study based on the DOX adsorption onto the Ti_3C_2@Fe_3O_4@β-CD was studied at different periods of time: 5, 10, 20, 30, 60, 90, 120, and 180 min, under the same batch conditions using 5 μg mL^{-1} DOX (pH 7.0) and individually mixed with Ti_3C_2@Fe_3O_4@β-CD (5 mg).

2.7. Desorption Experiments. Desorption experiments of DOX from Ti_3C_2@Fe_3O_4@β-CD was monitored that DOX-adsorbed Ti_3C_2@Fe_3O_4@β-CD was dispersed in ∼5 mL of phosphate buffer solution (PBS) with pH 9.0. The experiment was carried out in an orbital shaker and maintained at 160 rpm for 30 min. Then, the supernatant was completely separated from the mixture solution using an NdFeB strong magnet for data analysis by UV−visible spectrophotometer at 483 nm.

2.8. Characterization. The morphologies of Ti_3C_2 and Ti_3C_2@Fe_3O_4@β-CD were obtained by SEM and TEM and are presented in Figure 2. Figure 2a, b illustrates the typical Ti_3C_2 MXene with the layered structure. After being etched, the tightly packed layers are obviously separated from each other and transformed into a loose accordion-like structure with a significant layer spacing because of the loss of Al

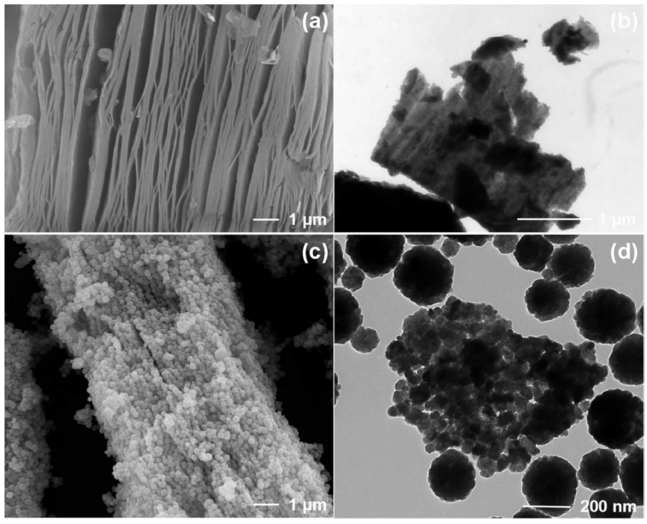

Figure 2. SEM images and TEM images of (a and b) Ti_3C_2 and (c and d) Ti_3C_2@Fe_3O_4@β-CD.

atoms.[36] After the incorporation of Fe_3O_4, a large number of regular spherical particles were immobilized uniformly into the structure of MXene nanosheets. Because of the thiol-ene click reaction between −SH of MPTMS and C═C of allyl-β-CD, the surface roughness of Ti_3C_2@Fe_3O_4@β-CD was increased (Figure 2c, d).

The groups and structure of Ti_3C_2, Ti_3C_2@Fe_3O_4, and Ti_3C_2@Fe_3O_4@β-CD were characterized by FT-IR analysis. As shown in Figure 3, the strong peaks of 3440, 1100, and 598

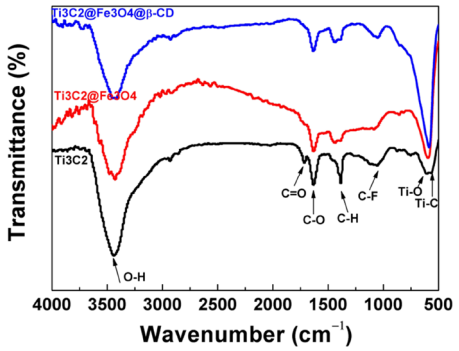

Figure 3. FT-IR spectra of Ti_3C_2, Ti_3C_2@Fe_3O_4, and Ti_3C_2@Fe_3O_4@β-CD.

cm^{-1} were measured in Ti_3C_2@Fe_3O_4 and Ti_3C_2@Fe_3O_4@β-CD, which should be from the stretching vibration of O−H, C−F, and Fe−O−Fe, respectively.[37] The O−H stretching vibration peak at 3440 cm^{-1} exhibited a typical large red-shift relative to that of free O−H mode. Accordingly, it is reasonable to suppose that β-CD coexisted in the magnetic nanomaterial. In particular, the vibration of the Ti−O bond may account for the peak at 663 cm^{-1}.[38] Thus, the Ti_3C_2, Ti_3C_2@Fe_3O_4, and Ti_3C_2@Fe_3O_4@β-CD have been successfully synthesized.

The crystal structures of Ti_3C_2, Ti_3C_2@Fe_3O_4, Ti_3C_2@Fe_3O_4@β-CD, Fe_3O_4, and Ti_3AlC_2 were investigated by XRD. As depicted in Figure 4, Fe_3O_4, Ti_3C_2@Fe_3O_4, and Ti_3C_2@Fe_3O_4@β-CD show similar diffraction patterns. Six characteristic peaks (2θ = 30.09, 35.47, 43.11, 53.61, 56.95, and 62.63°) were indexed to (220), (311), (400), (422), (511), and (440),

https://doi.org/10.1021/acsomega.2c02772
ACS Omega 2022, 7, 31945−31953

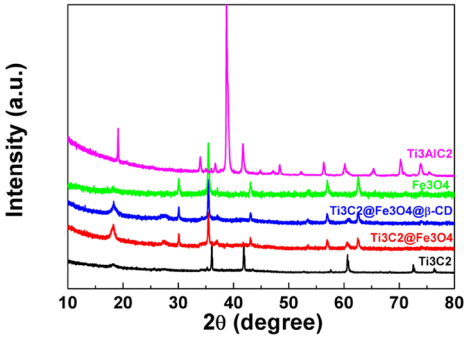

Figure 4. XRD patterns of Ti_3C_2, Ti_3C_2@Fe_3O_4, Ti_3C_2@Fe_3O_4@β-CD, Fe_3O_4, and Ti_3AlC_2.

respectively,[39] which match the face center cubic phase of Fe_3O_4 (JCPDS Card No. 19-629). There are a set of characteristic peaks at 2θ = 19.11, 33.96, 38.74, 41.76, and 60.18°, which corresponded to the (004), (101), (104), (105), and (109) planes of the Ti_3AlC_2 MAX phase.[40] Three peaks in the Ti_3C_2 MXene XRD pattern at 2θ = 18.27, 33.96, and 60.18° were observed. However, the peak at 38.74° (104) disappeared completely in the XRD pattern of the obtained Ti_3C_2 MXene nanosheets, which revealed that the aluminum phase in Ti_3AlC_2 MAX was exfoliated during the etching process.[41] Thus, the nanosheet structure of Ti_3C_2 MXene was successfully formed. Moreover, the (004) peak of the Ti_3C_2 MXene shifted toward the low-angle direction, which suggested the expansion of the MXene interlayer distance.[42] The characteristic diffraction peaks at 18.27, 33.96, and 60.18° in Ti_3C_2@Fe_3O_4 and Ti_3C_2@Fe_3O_4@β-CD were attributed to the crystal planes (004), (101), and (109) of Ti_3C_2 MXene, respectively. The above results further demonstrated that Ti_3C_2@Fe_3O_4@β-CD maintain the primary structure of Ti_3C_2 MXenes.

Figure 5a demonstrated the survey XPS spectrum of Ti_3C_2 and Ti_3C_2@Fe_3O_4@β-CD, which mainly contained five elements corresponding to C, Ti, O, F, and Fe elements. The high-resolution XPS spectra of C 1s (Figure 5b) could be decomposed into four components. The peaks at 288.5, 286.3, 284.8, and 281.5 eV might be assigned as C═O, C−O, C−C, and C−Ti, respectively. The XPS spectra of O 1s are presented in Figure 5c. The peaks at 532.7, 531.0, and 530.0 eV were ascribed to the Ti−O, C═O, and C−O group, respectively. The Ti 2p spectra of Ti_3C_2@Fe_3O_4@β-CD (Figure 5d) were also studied. Four functional groups appeared at 464.6, 459.5, 458.3, and 454.9 eV, which were associated with Ti−O, Ti−O 2p1/2, Ti−O 2p3/2, and Ti−C, respectively.[43,44] In addition, the relative elemental compositions of Ti_3C_2 and Ti_3C_2@Fe_3O_4@β-CD are summarized in Table 1. The relative content

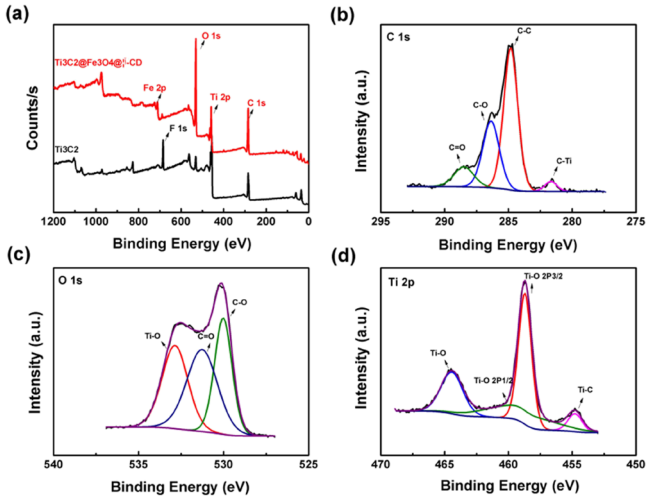

Figure 5. Survey spectra of (a) Ti_3C_2 and Ti_3C_2@Fe_3O_4@β-CD; (b) C 1s XPS spectra of Ti_3C_2@Fe_3O_4@β-CD; (c) O 1s XPS spectra of Ti_3C_2@Fe_3O_4@β-CD; (d) Ti 2p XPS spectra of Ti_3C_2@Fe_3O_4@β-CD.

Table 1. Elemental Compositions and Relative Contents of Ti_3C_2 and Ti_3C_2@Fe_3O_4@β-CD

materials	elemental compositions (%)				
	Fe 2p	O 1s	Ti 2p	C 1s	N 1s
Ti_3C_2	0.06	43.78	35.71	19.88	0.56
Ti_3C_2@Fe_3O_4@β-CD	11.80	47.18	20.92	19.46	0.64

of Fe 2p and O 1s increased obviously compared with Ti_3C_2 but Ti 2p decreased. The results further indicated that Ti_3C_2@Fe_3O_4@β-CD was successfully synthesized.

Figure 6 illustrates the magnetization curves of Fe_3O_4, Ti_3C_2@Fe_3O_4, and Ti_3C_2@Fe_3O_4@β-CD, and the saturation

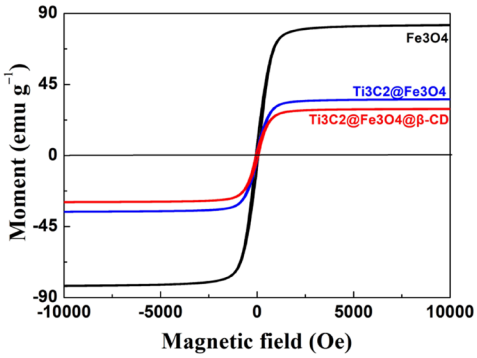

Figure 6. Magnetization curve of Fe_3O_4, Ti_3C_2@Fe_3O_4, and Ti_3C_2@Fe_3O_4@β-CD.

magnetization values were calculated to be about 82.61, 35.57, and 29.48 emu g^{-1}, respectively. The results demonstrated that three samples have magnetic properties and they can be readily separated from the reaction media. The saturation magnetization of the Ti_3C_2@Fe_3O_4@β-CD was lower than that of two others, mainly due to the introduction of Ti_3C_2 and β-CD.

Figure 7 shows the weight losses of Ti_3C_2@Fe_3O_4@β-CD upon heating under air atmosphere from 10 to 1000 °C. Under the low temperature, it may be caused by the evaporation of free water adsorbed on the surface of Ti_3C_2@Fe_3O_4@β-CD nanomaterials. Under the high temperature, it may be caused by the functional groups of Ti_3C_2@Fe_3O_4@β-CD. The less weight loss indicated that Ti_3C_2@Fe_3O_4@β-CD showed remarked thermogravimetric stability.

3. RESULTS AND DISCUSSION

3.1. Optimization of Adsorption Conditions. Figure 8a depicts that the adsorption percentage of DOX onto the Ti_3C_2@Fe_3O_4@β-CD varies with the sample pH. The adsorption percentage increased from 10.79 to 34.87% when the pH enhanced from 2.0 to 7.0. The reason may be that the Ti_3C_2@Fe_3O_4@β-CD surface was positively charged when

https://doi.org/10.1021/acsomega.2c02772
ACS Omega 2022, 7, 31945−31953

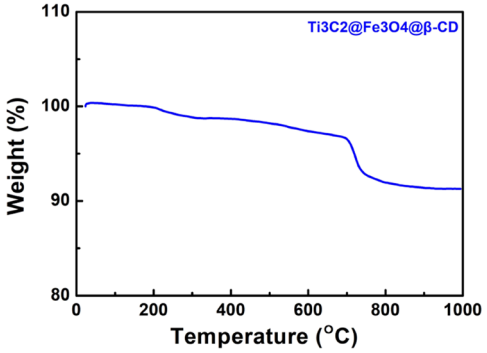

Figure 7. TGA thermogram of Ti_3C_2@Fe_3O_4@β-CD.

sample pH was low (pH_{PZC} is about 6.5); meanwhile, the electrostatic repulsion existed between DOX and Ti_3C_2@Fe_3O_4@β-CD surface.[9] Besides, a competition between H^+ ions and positively charged DOX molecules existing in the solution was presented on the surface of Ti_3C_2@Fe_3O_4@β-CD[14]. With increased pH, the electrostatic repulsion will decrease. The molecular structure of DOX contains −OH and $-NH_2$ groups, which can form hydrogen bonds with C═O and −OH groups on the surface of Ti_3C_2@Fe_3O_4@β-CD. The hydrogen-bonding interaction formed under natural conditions is stronger than that formed under acidic conditions. Regarding the structure and color alteration of DOX at the pH above 8.5, the adsorption percentage decreased obviously.[17] Thus, pH 7.0 was chosen in further experiments.

The influence of adsorption time was evaluated in the range of 5−180 min, as shown in Figure 8b. The adsorption percentage can be obtained as 41% within 60 min and then increased by only 7% from 60 to 180 min, which indicated that longer adsorption time is of little significance for increasing the adsorption percentage. Thus, 60 min was adopted as the adsorption time for subsequent analysis.

Figure 8c describes the effect of different initial concentrations of DOX on the adsorption percentage. The results indicated that the adsorption percentage of DOX onto the Ti_3C_2@Fe_3O_4@β-CD increased observably when the initial concentration was increased from 2 to 15 $\mu g\ mL^{-1}$, but it increased slowly later.

3.2. Adsorption Kinetics. Adsorption kinetics experiments help understand the dynamics and mechanism of the adsorption process. The kinetic study of DOX is also essential for designing and modeling the adsorption process by selecting optimal parameter conditions. In order to study the adsorption kinetics of DOX on adsorbents, the experimental data were analyzed by pseudo-first-order and pseudo-second-order kinetics models.[45−47] The linear relationships are formed according to eqs 3 and 4,

$$\log(q_e - q_t) = \log q_e - \frac{k_1}{2.303}t \quad (3)$$

$$\frac{t}{q_t} = \frac{1}{k_2 q_e^{\ 2}} + \frac{t}{q_e}t \quad (4)$$

where q_e and q_t are the amounts of DOX adsorbed at equilibrium and at time t ($\mu g\ mg^{-1}$), respectively. k_1 and k_2 are the rate constant of the pseudo-first-order models (min^{-1}) and the pseudo-second-order models ($mg\ \mu g^{-1}\ min^{-1}$), respectively.[28,30]

The kinetic parameters for DOX adsorption onto the Ti_3C_2@Fe_3O_4@β-CD are illustrated in Table 2. The correlation factors for the pseudo-first-order kinetic plot was less than 0.99, whereas the pseudo-second-order kinetic plot exhibited correlation factors of 0.9960 for DOX adsorption. Pseudo-second-order rate constants q_e and k^2 were calculated to be 7.35 $\mu g\ mg^{-1}$ and 0.0144 $mg\ \mu g^{-1}\ min^{-1}$ under experimental conditions, which could be determined from the slope and intercept of the line. The fitted value of q_e was very close to the experimental value of q_e (7.12 $\mu g\ mg^{-1}$), which further verified that DOX adsorption onto the Ti_3C_2@Fe_3O_4@β-CD are of the pseudo-second-order model. This implied that DOX adsorption could be dominated by chemisorption rather than physical adsorption. Chemisorption could be a result of host−guest interactions between DOX and β-CD or hydrogen-bonding interactions between Ti_3C_2@Fe_3O_4@β-CD and DOX.

3.3. Adsorption Isotherms. Adsorption isotherms provide valuable information about adsorption behavior, surface properties, and affinity of DOX toward the adsorbent. The amount of DOX-adsorbed on the Ti_3C_2@Fe_3O_4@β-CD surface and the amount of DOX remaining in the solution at a fixed temperature and pH at equilibrium can be evaluated by isotherms. The equilibrium adsorption of the Ti_3C_2@Fe_3O_4@β-CD was analyzed using Langmuir and Freundlich adsorption isotherms.[35]

The Langmuir isotherm assumes monolayer adsorption on the homogeneous surface, where the adsorbed each adsorbate species has equal adsorption activation energy. The expression for the Langmuir isotherm is as follows:

$$\frac{C_e}{q_e} = \frac{1}{q_{max} b} + \frac{C_e}{q_{max}} \quad (5)$$

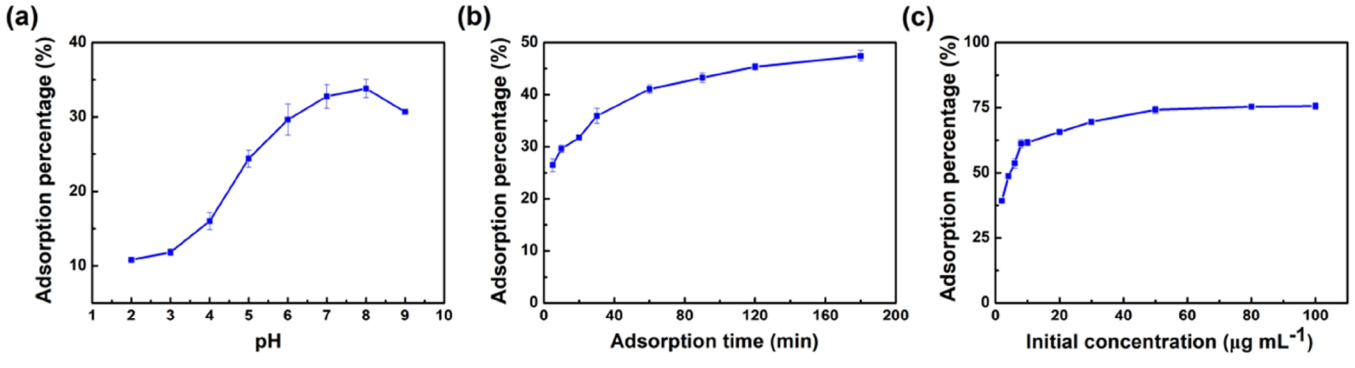

Figure 8. Effect of (a) pH; (b) adsorption time; and (c) initial concentration.

https://doi.org/10.1021/acsomega.2c02772
ACS Omega 2022, 7, 31945−31953

Table 2. Kinetic Parameters for the Adsorption of DOX onto the Ti_3C_2@Fe_3O_4@β-CD

	pseudo-first-order model			pseudo-second-order model		
$q_{e,exp}$ (μg mg^{-1})	k_1 (min^{-1})	$q_{e,cal}$ (μg mg^{-1})	R^2	k_2 (mg μg^{-1} min^{-1})	$q_{e,cal}$ (μg mg^{-1})	R^2
7.12	0.0018	15.95	0.9010	0.0144	7.35	0.9960

Table 3. Parameters of the Langmuir and Freundlich Isotherms for DOX Adsorption

Langmuir model				Freundlich model		
q_{max} (μg mg^{-1})	b (mL μg^{-1})	R^2	R_L	$1/n$	K	R^2
−90.09	−0.035	0.4934	−0.400−1.075	1.1424	2.194	0.9916

where C_e represents the equilibrium concentration of DOX in the supernatant (μg mL^{-1}); q_e is DOX uptake at the adsorption equilibrium per weight of the adsorbent (μg mg^{-1}); q_{max} is the maximum DOX adsorption capacity per weight of the adsorbent (μg mg^{-1}); and b is the Langmuir adsorption constant (mL μg^{-1}). The slope and intercept of the linear plot of C_e/q_e against C_e yield the values of q_{max} and b.[48]

Also, the Langmuir isotherm can be employed to predict whether or not an adsorption process is favorable by a dimensionless constant separation factor, R_L, which is represented as follows:

$$R_L = \frac{1}{1 + bC_0} \tag{6}$$

where C_0 is the initial concentration of DOX (μg mL^{-1}). The value of R_L indicates that the shape of the isotherm and is defined as follows: $R_L = 0$ (irreversible), $0 < R_L < 1$ (favorable), $R_L > 1$ (unfavorable), and $R_L = 1$ (linear).

The Freundlich isotherm is considered as model multilayer adsorption, which occurs on a heterogeneous surface, and its linear form can be expressed as follows:

$$\log(q_e) = \frac{1}{n}\log(C_e) + \log k \tag{7}$$

where k is the Freundlich constant indicative of adsorption capacity; $1/n$ is an empirical parameter that represents the adsorption capacity of the adsorbent and the energy of adsorption.[30,49] k and n can be obtained from the intercept and the slope of the linear plot of $\log(q_e)$ versus $\log(C_e)$, respectively. For the favorable adsorption process, the value of n should lie in the range of 1−10.

In this study, Langmuir and Freundlich isotherm models were fitted with experimental data, and then, the constants and correlation factors were calculated and listed in Table 3. Based on the correlation factor (R^2) values, it can be deduced that the adsorption process of DOX onto the Ti_3C_2@Fe_3O_4@β-CD followed the Freundlich isotherm model owing to a high correlation value of 0.9916. This implied that multilayer adsorption took place over the Ti_3C_2@Fe_3O_4@β-CD. The assumption for this isotherm is that the interaction between the adsorbent surface and adsorbed molecules occurs on a heterogeneous surface, and the energy is distributed non-uniformly. The Langmuir isotherm model did not correlate with the experimental data. The plot of C_e/q_e versus C_e does not follow a linear relationship, presenting a bad correlation coefficient (R^2 = 0.4934). It is apparent that the Langmuir model was unsuitable to describe the adsorption behaviors of DOX onto the Ti_3C_2@Fe_3O_4@β-CD.

3.4. Thermodynamic Studies. The adsorption behaviors of Ti_3C_2@Fe_3O_4@β-CD for DOX were critically investigated at 298, 308, and 318 K. Thermodynamic parameters are calculated from eqs 8, 9, and 10:[48]

$$\Delta G^0 = -RT \ln K_d \tag{8}$$

$$K_d = \frac{q_e}{C_e} \tag{9}$$

$$\ln K_d = \frac{\Delta S^0}{R} - \frac{\Delta H^0}{RT} \tag{10}$$

where K_d is the distribution coefficient; R is the ideal gas constant (8.314 J mol^{-1} K^{-1}); and T is the temperature (K). Gibbs free energy change (ΔG^0) was calculated using ln K_d values for different temperatures. Enthalpy change (ΔH^0) and entropy change (ΔS^0) are calculated from the slopes and intercepts of eq 10.

According to eq 10, the thermodynamic parameters were summarized in Table 4. The value of ΔH^0 confirmed that the DOX adsorption progress onto the Ti_3C_2@Fe_3O_4@β-CD was endothermic and the adsorption percentage of DOX increased with temperature. The value of ΔS^0 indicated a greater order of reaction during DOX adsorption and the negative values of ΔG^0 reflected the DOX adsorption progress onto the Ti_3C_2@Fe_3O_4@β-CD was a spontaneous and feasible process.

Table 4. Thermodynamic Parameters for Adsorption of DOX onto the Ti_3C_2@Fe_3O_4@β-CD

T/K	ΔG^0/kJ mol^{-1}	ΔH^0/kJ mol^{-1}	ΔS^0/J mol^{-1} K^{-1}
298	−2.68	11.63	48.05
308	−3.19		
318	−3.63		

3.5. Desorption and Regeneration. To investigate the possibility of Ti_3C_2@Fe_3O_4@β-CD regeneration, the desorption experiments were performed. The results showed that PBS solutions (pH 9.0) could be used for Ti_3C_2@Fe_3O_4@β-CD regeneration, and the desorption percentage was above 70%. The molecular structure of DOX contains −OH and $-NH_2$ groups, which can form hydrogen-bonding interactions with C═O and −OH groups on the surface of Ti_3C_2@Fe_3O_4@β-CD.[18,24] With pH increased, the hydrogen-bonding interaction was broken, which may result in the desorption of DOX from the surface of Ti_3C_2@Fe_3O_4@β-CD. The adsorption percentage remained in the range of 41.05−44.09%, and RSD based on the adsorption percentage through five replicate adsorption and desorption process was 2.8%. The desorption and regeneration results indicated that Ti_3C_2@Fe_3O_4@β-CD can be employed as a kind of recyclable adsorbents for DOX adsorption.

https://doi.org/10.1021/acsomega.2c02772
ACS Omega 2022, 7, 31945−31953

3.6. Interference Experiments. The interference on the adsorption of DOX was investigated when Na^+, Cl^-, NO_3^-, SO_4^{2-}, Co^{2+}, and Cu^{2+} ions as the interfering ions coexisted with DOX in solution. The tolerance of interfering ions is defined as a 5% reduction in signal intensity. Results in Table 5 showed that the interfering ions cause no significant interference with the determination of DOX of 5 $\mu g\ mL^{-1}$ at pH 7.0. This is probably because the chemisorption based on host−guest interactions and hydrogen-bonding interactions are the primary adsorption.

Table 5. Effect of Interfering Ions

coexisting ions	tolerance limit/$\mu g\ mL^{-1}$
Na^+, Cl^-	1000
SO_4^{2-}, NO_3^+, Cu^{2+}, Co^{2+}	100

3.7. Comparison of Ti_3C_2@Fe_3O_4@β-CD Performance with the Other Adsorbents. The comparisons of Ti_3C_2@Fe_3O_4@β-CD with other adsorbents for adsorption of DOX are summarized in Table 6. Higher adsorption capacities of some other's work are related to the higher initial concentration and more adsorbent dosage used in these studies than the presented work. However, the proposed method can offer several advantages, including that it does not require any expensive instruments, complex preparation steps, and the operation is much easier.

4. CONCLUSIONS

The synthesis procedure and structural characterization of Ti_3C_2@Fe_3O_4@β-CD and then Ti_3C_2@Fe_3O_4@β-CD as an efficient adsorbent to adsorb DOX from aqueous solutions are reported in the present work. SEM analysis confirmed that the surface of Ti_3C_2 MXene was obviously a loose accordion-like structure. After preparing Ti_3C_2@Fe_3O_4@β-CD, a large number of regular spherical particles were uniformly immobilized in the structure of MXene nanosheets. XRD analysis confirmed that Ti_3C_2@Fe_3O_4@β-CD maintains the primary structure of Ti_3C_2 MXenes and Fe_3O_4. VSM analysis demonstrated that the prepared materials had magnetic properties and they could be readily separated from the reaction media. TGA analysis indicated that Ti_3C_2@Fe_3O_4@β-CD possessed remarked thermogravimetric stability. The batch study confirmed that the adsorption of DOX onto the Ti_3C_2@Fe_3O_4@β-CD depended on the parameters such as pH, adsorption time, and initial concentration. Kinetic models and adsorption isotherms demonstrated that DOX adsorption fitted well to the pseudo-second-order kinetics models and Freundlich isotherm models. The thermodynamic study indicated that DOX adsorption onto the Ti_3C_2@Fe_3O_4@β-CD was endothermic, and the negative ΔG^0 values implied spontaneous adsorption. The positive value of ΔS^0 showed that randomness increased at the solid/solution interface. Moreover, Ti_3C_2@Fe_3O_4@β-CD could be effectively regenerated using a solution of PBS (pH 9.0). The adsorption percentage remained in the range of 41.05−44.09%, and RSD based on the adsorption percentage through five replicate adsorption and desorption process was 2.8%. These remarkable results indicated that Ti_3C_2@Fe_3O_4@β-CD possessed potential applications to adsorb DOX from aqueous solutions.

AUTHOR INFORMATION

Corresponding Author

Dan Liu − *School of Chemistry and Chemical Engineering, Jiangsu University of Technology, Changzhou 213001, China*; orcid.org/0000-0002-0425-8039; Email: liudan@jsut.edu.cn

Authors

Tongyi Li − *School of Chemistry and Chemical Engineering, Jiangsu University of Technology, Changzhou 213001, China*

Wenjie Sun − *School of Chemistry and Chemical Engineering, Jiangsu University of Technology, Changzhou 213001, China*

Wenjuan Zhou − *School of Chemistry and Chemical Engineering, Jiangsu University of Technology, Changzhou 213001, China*

Guohua Zhang − *School of Chemistry and Chemical Engineering, Jiangsu University of Technology, Changzhou 213001, China*

Complete contact information is available at: https://pubs.acs.org/10.1021/acsomega.2c02772

Notes

The authors declare no competing financial interest.

ACKNOWLEDGMENTS

The authors are thankful to the Analysis and Testing Center of Jiangsu University of Technology for providing instruments to conduct and complete this study.

REFERENCES

(1) Kong, F. Y.; He, X. D.; Liu, Q. Q.; Qi, X. X.; Sun, D. D.; Zheng, Y. T.; Wang, R. G.; Bai, Y. L. Further surface modification by carbon coating for in-situ growth of Fe_3O_4 nanoparticles on MXene Ti_3C_2 multilayers for advanced Li-ion storage. *Electrochim. Acta* **2018**, *289*, 228−237.

(2) Xue, Q.; Zhang, H. J.; Zhu, M. S.; Pei, Z. X.; Li, H. F.; Wang, Z. F.; Huang, Y.; Huang, Y.; Deng, Q. H.; Zhou, J.; Du, S. Y.; Huang, Q.; Zhi, C. Y. Photoluminescent Ti_3C_2 MXene quantum dots for multicolor cellular imaging. *Adv. Mater.* **2017**, *29*, No. 1604847.

Table 6. Comparison of Ti_3C_2@Fe_3O_4@β-CD with Other Adsorbents Applied for Adsorption of DOX

adsorbents	pH	initial concentration ($mg\ mL^{-1}$)	temperature (°C)	adsorbent dosage	adsorption capacity	adsorption time	ref
GO@Fe_3O_4@ZnO@CS	7.0	10	25	0.01 g	390 $mg\ g^{-1}$	45 min	14
green magnetic/graphene oxide/chitosan/alliumsativum/quercus nanocomposite	6.3	2		1.4 $g\ L^{-1}$		10 min	9
Fe_3O_4 NPs	6.0	20	30	0.5 $g\ L^{-1}$	32 $mg\ g^{-1}$	48 h	18
Fe_3O_4@SiO_2-Glu	7.4	20	30	10 mg	64.51 $mg\ g^{-1}$	24 h	17
Ti_3C_2@Fe_3O_4@β-CD	7.0	5	25	5 mg	7.35 $\mu g\ mg^{-1}$	60 min	this work

https://doi.org/10.1021/acsomega.2c02772
ACS Omega 2022, 7, 31945−31953

(3) Fang, Y. F.; Yang, X. C.; Chen, T.; Xu, G. F.; Liu, M. L.; Liu, J. Q.; Xu, Y. H. Two-dimensional titanium carbide (MXene)-based solid-state electrochemiluminescent sensor for label-free single-nucleotide mismatch discrimination in human urine. *Sens. Actuators, B* **2018**, *263*, 400−407.
(4) Chen, X.; Sun, X. K.; Xu, W.; Pan, G. C.; Zhou, D. L.; Zhu, J. Y.; Wang, H.; Bai, X.; Dong, B.; Song, H. W. Ratiometric photoluminescence sensing based on Ti_3C_2 MXene quantum dots as an intracellular pH sensor. *Nanoscale* **2018**, *10*, 1111−1118.
(5) Zhang, Q. R.; Teng, J.; Zou, G. D.; Peng, Q. M.; Du, Q.; Jiao, T. F.; Xiang, J. Y. Efficient phosphate sequestration for water purification by unique sandwich-like MXene/magnetic iron oxide nanocomposites. *Nanoscale* **2016**, *8*, 7085−7093.
(6) Yaqub, A.; Shafiq, Q.; Khan, A. R.; Husnain, S. M.; Shahzad, F. Recent advances in the adsorptive remediation of wastewater using two-dimensional transition metal carbides (MXenes): a review. *New J. Chem.* **2021**, *45*, 9721−9742.
(7) Ghani, A. A.; Shahzad, A.; Moztahida, M.; Tahir, K.; Jeon, H.; Kim, B.; Lee, D. S. Adsorption and electrochemical regeneration of intercalated $Ti_3C_2T_x$ MXene for the removal of ciprofloxacin from wastewater. *Chem. Eng. J.* **2021**, *421*, No. 127780.
(8) Kong, A. Q.; Sun, Y. W.; Peng, M.; Gu, H. Z.; Fu, Y.; Zhang, J. L.; Li, W. Amino-functionalized MXenes for efficient removal of Cr(VI). *Colloids Surf., A* **2021**, *617*, No. 126388.
(9) Arjmand, O.; Ardjmand, M.; Amani, A. M.; Eikani, M. H. Effective adsorption of doxorubicin hydrochloride on the green targeted nanocomposite. *Acta Chim. Slov.* **2020**, *67*, 496−506.
(10) Shi, Y. Q.; Wang, Y. X.; Zhu, J. H.; Liu, W.; Khan, M. Z. H.; Liu, X. H. Molecularly imprinting polymers (MIP) based on nitrogen doped carbon dots and mIL-101(Fe) for doxorubicin hydrochloride delivery. *Nanomaterials* **2020**, *10*, 1655.
(11) Mahnik, S. N.; Lenz, K.; Weissenbacher, N.; Mader, R. M.; Fuerhacker, M. Fate of 5-fluorouracil, doxorubicin, epirubicin, and daunorubicin in hospital wastewater and their elimination by activated sludge and treatment in a membrane-bio-reactor system. *Chemosphere* **2007**, *66*, 30−37.
(12) Martín, J.; Camacho-Muñoz, D.; Santos, J. L.; Aparicio, I.; Alonso, E. Occurrence and ecotoxicological risk assessment of 14 cytostatic drugs in wastewater. *Water, Air, Soil Pollut.* **2014**, *225*, 1896.
(13) Kelbert, M.; Pereira, C. S.; Daronch, N. A.; Cesca, K.; Michels, C.; de Oliveira, D.; Soares, H. M. Laccase as an efficacious approach to remove anticancer drugs: A study of doxorubicin degradation, kinetic parameters, and toxicity assessment. *J. Hazard. Mater.* **2021**, *409*, No. 124520.
(14) Cheraghi, M.; Lorestani, B.; Zandipak, R.; Sobhanardakani, S. GO@Fe_3O_4@ZnO@CS nanocomposite as a novel adsorbent for removal of doxorubicin hydrochloride from aqueous solutions. *Toxin Rev.* **2022**, 1−10.
(15) Landry, K. A.; Boyer, T. H. Diclofenac removal in urine using strong-base anion exchange polymer resins. *Water Res.* **2013**, *47*, 6432−6444.
(16) Gao, L.; He, Q.; Xing, J.; Ge, Z. Removal of doxorubicin by magnetic copper phosphate nanoflowers for individual urine source separation. *Chemosphere* **2020**, *238*, No. 124690.
(17) Cai, W. L.; Guo, M. Y.; Weng, X. L.; Zhang, W.; Chen, Z. L. Adsorption of doxorubicin hydrochloride on glutaric anhydride functionalized Fe_3O_4@SiO_2 magnetic nanoparticles. *Mater. Sci. Eng., C* **2019**, *98*, 65−73.
(18) Weng, X. L.; Ma, L.; Guo, M. Y. U.; Su, Y. Y.; Dharmarajan, R.; Chen, Z. L. Removal of doxorubicin hydrochloride using Fe_3O_4 nanoparticles synthesized by euphorbia cochinchinensis extract. *Chem. Eng. J.* **2018**, *353*, 482−489.
(19) Fu, H. Y.; Wang, R. Z.; Xu, Q. Y.; Laipan, M.; Tang, C. L.; Zhang, W. X.; Ling, L. Facile construction of Fe/Pd-doped graphite carbon nitride for effective removal of doxorubicin: Performance, mechanism and degradation pathways. *Appl. Catal., B* **2021**, *299*, No. 120686.
(20) Arabian, T.; Amjad-Iranagh, S.; Halladj, R. Molecular dynamics simulation study of doxorubicin adsorption on functionalized carbon nanotubes with folic acid and tryptophan. *Sci. Rep.* **2021**, *11*, 24210.
(21) Sadrnia, A.; Orooji, Y.; Behmaneshfar, A.; Darabi, R.; Maghsoudlou Kamali, D.; Karimi-Maleh, H.; Opoku, F.; Govender, P. P. Developing a simple box-behnken experimental design on the removal of doxorubicin anticancer drug using Fe_3O_4/graphene nanoribbons adsorbent. *Environ. Res.* **2021**, *200*, No. 111522.
(22) Teng, Y.; Du, Y. M.; Shi, J.; Pong, P. W. T. Magnetic iron oxide nanoparticle-hollow mesoporous silica Spheres: Fabrication and potential application in drug delivery. *Curr. Appl. Phys.* **2020**, *20*, 320−325.
(23) Lucaci, A.-R.; Bulgariu, D.; Bulgariu, L. In situ functionalization of iron oxide particles with alginate: a promising biosorbent for retention of metal ions. *Polymer* **2021**, *13*, 3554.
(24) Cai, W. L.; Guo, M. Y.; Weng, X. L.; Zhang, W.; Owens, G.; Chen, Z. L. Modified green synthesis of Fe_3O_4@SiO_2 nanoparticles for pH responsive drug release. *Mater. Sci. Eng., C* **2020**, *112*, No. 110900.
(25) Han, J. J.; Wang, H. Q.; Li, Z. F.; Wang, Z. H. Preparation of chitosan-modified magnetic Schiff base network composite nanospheres for effective enrichment and detection of hippuric acid and 4-methyl hippuric acid. *J. Chromatogr., A* **2021**, *1652*, No. 462373.
(26) Xiong, F.; Jia, J.; Ma, J.; Jia, Q. Glutathione-functionalized magnetic thioether-COFs for the simultaneous capture of urinary exosomes and enrichment of exosomal glycosylated and phosphorylated peptides. *Nanoscale* **2022**, *14*, 853−864.
(27) Jiang, D. D.; Li, X. Q.; Jia, Q. Multilayer cucurbit[6]uril-based magnetic nanoparticles prepared by host-guest interaction: remarkable adsorbent for low density lipoprotein removal from plasma. *Chem. − Eur. J.* **2018**, *24*, 2242−2248.
(28) Zhang, W.; Zhang, Y. M.; Liu, Y. Cyclodextrin-cross-linked hydrogels for adsorption and photodegradation of cationic dyes in aqueous solution. *Chem. − Asian J.* **2021**, *16*, 1−8.
(29) Liu, K.; Liu, H. J.; Li, L. X.; Li, W.; Liu, J.; Tang, T. Adsorption of methyl violet from aqueous solution using *β*-cyclodextrin immobilised onto mesoporous silica. *Supramol. Chem.* **2021**, *33*, 107−121.
(30) Usman, M.; Ahmed, A.; Ji, Z. J.; Yu, B.; Shen, Y. Q.; Cong, H. L. Environmentally friendly fabrication of new beta-Cyclodextrin/ZrO_2 nanocomposite for simultaneous removal of Pb(II) and BPA from water. *Sci. Total Environ.* **2021**, *784*, No. 147207.
(31) Kekes, T.; Kolliopoulos, G.; Tzia, C. Hexavalent chromium adsorption onto crosslinked chitosan and chitosan/*β*-cyclodextrin beads: Novel materials for water decontamination. *J. Environ. Chem. Eng.* **2021**, *9*, No. 105581.
(32) Haji, A.; Khajeh Mehrizi, M.; Sarani, M. Surface modification of polypropylene nonwoven by plasma and *β*-cyclodextrin: optimization and cationic dye removal studies. *Surf. Interface* **2021**, *25*, No. 101278.
(33) Liu, D.; Tan, H. P.; Meng, L. L.; Jia, H. L.; Zhou, W. J.; Wu, H. Y. Preparation of cysteine-functionalized Fe_3O_4 magnetic nanoparticles for determination of Cu^{2+}. *ChemistrySelect* **2021**, *6*, 6683−6689.
(34) Zheng, H. J.; Liu, Q. W.; Jia, Q. Preparation of poly(butyl methacrylate-*co*-ethyleneglyceldimethacrylate) monolithic column modified with beta-cyclodextrin and nano-cuprous oxide and its application in polymer monolithic microextraction of polychlorinated biphenyls. *J. Chromatogr., A* **2014**, *1343*, 47−54.
(35) Deb, A. K.; Biswas, B.; Naidu, R.; Rahman, M. M. Mechanistic insights of hexavalent chromium remediation by halloysite-supported copper nanoclusters. *J. Hazard. Mater.* **2022**, *421*, No. 126812.
(36) Song, T.; Hou, L. Q.; Long, B.; Ali, A.; Deng, G. J. Ultrathin MXene "bridge" to accelerate charge transfer in ultrathin metal-free 0D/2D black phosphorus/g-C_3N_4 heterojunction toward photocatalytic hydrogen production. *J. Colloid Interface Sci.* **2021**, *584*, 474−483.
(37) Luo, Z. F.; Xu, M. W.; Wang, R. Z.; Liu, X. B.; Huang, Y. K.; Xiao, L. T. Magnetic Ti_3C_2 MXene functionalized with beta-cyclodextrin as magnetic solid-phase extraction and in situ

https://doi.org/10.1021/acsomega.2c02772
ACS Omega 2022, 7, 31945−31953

derivatization for determining 12 phytohormones in oilseeds by ultra-performance liquid chromatography-tandem mass spectrometry. *Phytochemistry* **2021**, *183*, No. 112611.
(38) Liu, M. W.; Zhou, J.; He, Y.; Cai, Z. X.; Ge, Y. L.; Zhou, J. G.; Song, G. W. ϵ-poly-L-lysine-protected Ti_3C_2 MXene quantum dots with high quantum yield for fluorometric determination of cytochrome c and trypsin. *Microchim. Acta* **2019**, *186*, 770.
(39) Zare, M.; Sarkati, M. N. Chitosan-functionalized Fe_3O_4 nanoparticles as an excellent biocompatible nanocarrier for silymarin delivery. *Polym. Adv. Technol.* **2021**, 1−7.
(40) Ke, T.; Shen, S. Y.; Rajavel, K.; Yang, K.; Lin, D. H. In situ growth of TiO_2 nanoparticles on nitrogen-doped Ti_3C_2 with isopropyl amine toward enhanced photocatalytic activity. *J. Hazard. Mater.* **2021**, *402*, No. 124066.
(41) Deng, B. W.; Liu, Z. C.; Pan, F.; Xiang, Z.; Zhang, X.; Lu, W. Electrostatically self-assembled two-dimensional magnetized MXene/hollow Fe_3O_4 nanoparticle hybrids with high electromagnetic absorption performance and improved impendence matching. *J. Mater. Chem. A* **2021**, *9*, 3500−3510.
(42) Chen, R. H.; Cheng, Y. Y.; Wang, P.; Wang, Y. Y.; Wang, Q. W.; Yang, Z. H.; Tang, C. J.; Xiang, S. Y.; Luo, S. Y.; Huang, S. H.; Su, C. Q. Facile synthesis of a sandwiched $Ti_3C_2T_x$ MXene/nZVI/fungal hypha nanofiber hybrid membrane for enhanced removal of Be(II) from $Be(NH_2)_2$ complexing solutions. *Chem. Eng. J.* **2021**, *421*, No. 129682.
(43) Ranjith, K. S.; Ezhil Vilian, A. T.; Ghoreishian, S. M.; Umapathi, R.; Hwang, S. K.; Oh, C. W.; Huh, Y. S.; Han, Y. K. Hybridized 1D-2D $MnMoO_4$-MXene nanocomposites as high-performing electrochemical sensing platform for the sensitive detection of dihydroxybenzene isomers in wastewater samples. *J. Hazard. Mater.* **2022**, *421*, No. 126775.
(44) Zhong, W.; Gao, F.; Zou, J.; Liu, S. W.; Li, M. F.; Gao, Y. S.; Yu, Y. F.; Wang, X. Q.; Lu, L. M. MXene@Ag-based ratiometric electrochemical sensing strategy for effective detection of carbendazim in vegetable samples. *Food Chem.* **2021**, *360*, No. 130006.
(45) Zhou, Y. Z.; Luan, L. P.; Tang, B. T.; Niu, Y. Z.; Qu, R. J.; Liu, Y.; Xu, W. L. Fabrication of Schiff base decorated PAMAM dendrimer/magnetic Fe_3O_4 for selective removal of aqueous Hg(II). *Chem. Eng. J.* **2020**, *398*, No. 125651.
(46) Chen, Z. C.; Tang, B. T.; Niu, Y. Z.; Chen, H.; Liu, Y. F.; Wang, A. L.; Bai, L. J. Synthesis of silica supported thiosemicarbazide for Cu(II) and Zn(II) adsorption from ethanol: A comparison with aqueous solution. *Fuel* **2021**, *286*, No. 119287.
(47) Luan, L. P.; Tang, B. T.; Liu, Y. F.; Wang, A. L.; Zhang, B. B.; Xu, W. L.; Niu, Y. Z. Selective capture of Hg(II) and Ag(I) from water by sulfur-functionalized polyamidoamine dendrimer/magnetic Fe_3O_4 hybrid materials. *Sep. Purif. Technol.* **2021**, *257*, No. 117902.
(48) Xu, M. W.; Huang, C. H.; Lu, J.; Wu, Z. H.; Zhu, X. X.; Li, H.; Xiao, L. T.; Luo, Z. F. Optimizing adsorption of 17α-ethinylestradiol from water by magnetic MXene using response surface methodology and adsorption Kinetics, Isotherm, and Thermodynamics studies. *Molecules* **2021**, *26*, 3150.
(49) Sun, B.; Dong, X. S.; Li, H. P.; Shang, Y. P.; Zhang, Y. X.; Hu, F. L.; Gu, S. N.; Wu, Y.; Gao, T. Y.; Zhou, G. W. Surface charge engineering for two-dimensional Ti_2CT_x MXene for highly efficient and selective removal of cationic dye from aqueous solution. *Sep. Purif. Technol.* **2021**, *272*, No. 118964.

https://doi.org/10.1021/acsomega.2c02772
ACS Omega 2022, 7, 31945−31953